INTERNATIONAL JOURNAL OF
NUMERICAL ANALYSIS AND MODELING
Volume 6, Number 4, Pages 562–585

FRONT TRACKING ALGORITHM FOR THE LIGHTHILL-WHITHAM-RICHARDS TRAFFIC FLOW MODEL WITH A PIECEWISE QUADRATIC, CONTINUOUS, NON-SMOOTH, AND NON-CONCAVE FUNDAMENTAL DIAGRAM

WENQIN CHEN, S.C. WONG, CHI-WANG SHU, AND PENG ZHANG

Abstract. We use a front tracking algorithm to explicitly construct entropy solutions for the Lighthill-Whitham-Richards traffic flow model with a flow-density relationship that is piecewise quadratic, continuous, non-smooth, and non-concave. The solution is exact if the initial condition is piecewise linear and the boundary conditions are piecewise constant. The algorithm serves as a fast and accurate solution tool for the prediction of spatio-temporal traffic conditions and as a diagnostic tool for testing the performance of numerical schemes. Numerical examples are used to illustrate the effectiveness and efficiency of the proposed method relative to numerical solutions that are obtained using a fifth-order weighted essentially non-oscillatory scheme.

Key words. LWR model, traffic flow, piecewise quadratic fundamental diagram, front tracking algorithm, WENO scheme.

1. INTRODUCTION

Lighthill and Whitham [23] provided one of the first published theories of the macroscopic modeling of highway traffic flow. Their theory was based on two relationships: a continuity equation and the fundamental relationship between the flow and density of a traffic stream. The continuity equation can easily be derived by considering the conservation of vehicles between any two locations on a road, which is why it is often called a conservation equation. As an assumed speed-density relationship is needed to solve and apply the continuity equation for traffic flow, studies on the relationships between the fundamental traffic stream variables are vital, and have been provided throughout the history of traffic flow study. With the continuity equation, a speed-density relationship, and the initial and boundary conditions of the traffic stream, the density at any location along a road can be determined. Richards [30] independently proposed the same continuum approach, albeit in a slightly different form. The key difference is that Richards focused on the derivation of shock waves with respect to density, whereas Lighthill and Whitham considered the same from the perspective of disruptions to traffic flow. Another difference between the two methods is that Richards adopted a linear speed-density relationship, whereas Lighthill and Whitham used a more general speed-density relationship. Because of the nearly simultaneous and independent development of the theory, the model has become known in the literature as the LWR model.

The LWR model, as a scalar hyperbolic conservation law, can be solved by approximating the fundamental diagram (or flux function) as a piecewise linear function [3], in which the solution of the Riemann problem is a step function (piecewise

Received by the editors February 29, 2008 and, in revised form, February 4, 2009.
2000 *Mathematics Subject Classification.* 35R35, 49J40, 60G40.
This research was supported by grants from the Research Grants Council of the Hong Kong Special Administrative Region, China (Project No.: HKU7187/05E), the University of Hong Kong (10207394), the National Natural Science Foundation of China (70629001, 10671190, 10771134), and the National Basic Research Program of China (2006CB705500).

constants). If the initial data falls within the class of step functions, then an analytical solution of the Cauchy problem can be constructed by the superposition of simple Riemann problems. The solution will always remain piecewise constant, and will therefore always be within the same class of functions, because all wave interactions lead to new Riemann problems. By solving the Riemann problems that arise each time two or more waves interact, a global solution can be established. In the general case, approximating the flux function by a sequence of piecewise linear functions and the initial data by a sequence of step functions gives a compact sequence of approximate solutions that converge to the solution of the Cauchy problem. Similarly, Newell [27–29] assumed a triangular or trapezoidal shape of the fundamental diagram and proposed a simple graphical procedure to derive the analytical solution to the LWR model on incident detection using the concept of cumulative flow. These studies unintentionally share the same rationale as Dafermos' method. More recently, and inspired by Dafermos, Henn [6, 7] proposed a solution algorithm for the LWR model known as the wave tracking scheme that is based both on the piecewise linear approximation of the fundamental flow-density relationship and on an explicit tracking of waves, and further implemented the scheme to evaluate the impact of incidents on the road.

Lucier [26] extended Dafermos' method to approximate the flux function using a parabolic spline approximation, in which the piecewise quadratic functions are continuously differentiable with discontinuous second derivatives at the breakpoints. Holden et al. [8, 9] enhanced Dafermos' method and showed that even in infinite time, there are only a finite number of constant states. They also proved that the construction is well defined for non-convex flux functions. They called the method front tracking – front referring to the discontinuities and tracking to the process of computing collisions and resolving interactions. Front tracking has proved to be a very robust numerical method for scalar, one-dimensional conservation laws. Kunick [21] proved an explicit representation formula for the solution of a one-dimensional hyperbolic conservation law with a non-convex flux function but monotone initial data based on the polygonal method of Dafermos. Other developments and applications of the front tracking method can also be found in [1, 11, 14–17].

Unaware of the earlier development of the front tracking method [10], Wong and Wong [35] rediscovered the method of Lucier [26] for solving a scalar hyperbolic conservation law, and determined the formation and propagation of shocks on a homogeneous highway subject to general boundary conditions assuming a linear speed-density relationship (or parabolic flux function). The method of Wong and Wong [35] can therefore be considered to be a special case of the method of Lucier [26] in which the solution is exact if the fundamental diagram is a parabolic flux function, the initial condition is piecewise linear, and the boundary conditions are piecewise constant. In both Wong and Wong [35] and Lucier [26], explicit expressions that describe the relationship between the density, space, and time of different scenarios (characteristics, fan, and shock) were derived to allow the evolution of traffic density in space and time to be precisely determined, although Lucier's focus was on the theoretical proof of the convergence rate of the algorithm when a general flux function is approximated by a number of piecewise quadratic functions. More recently, Lu et al. [25] proposed an improved front tracking algorithm that adopts a piecewise quadratic, continuous, and concave fundamental diagram. As their algorithm does not require the piecewise quadratic function to be continuously differentiable at the junction points, they improved on the method proposed

both by Lucier and by Wong and Wong by relaxing the restrictive differentiability assumptions on the fundamental diagram.

However, the algorithm of Lu et al. requires the piecewise quadratic fundamental diagram to be globally concave, although it can be non-smooth at the junction points. This is still too strong for representing realistic traffic conditions, because it is often observed from field data that the fundamental diagram is not globally concave, but only locally concave and even convex in different density regimes (see early works by Underwood [32] and Drake et al. [4] for calibrated non-concave fundamental diagrams based on observed data). Non-concave fundamental diagrams have also been widely used by theoreticians for modeling traffic flow [4, 18, 19, 34]. It will therefore be useful to investigate the entropy solutions to the LWR model with a non-smooth and non-concave flow-density relationship.

In this paper, we present explicit formulae for entropy solutions with a piecewise quadratic, continuous, non-smooth and non-concave flow-density relationship and a piecewise linear initial condition and piecewise constant boundary conditions. The remainder of the paper is organized as follows. Sections 2 and 3 develop explicit formulas for the entropy solutions with the aforementioned flow-density relationship and with a piecewise linear initial condition and piecewise constant boundary conditions. In Section 4, we summarize the solution procedure, concentrating on finding the earliest time when the waves (characteristics or shocks) from the previous initial condition intersect with one another, at which point the construction of the entropy solution must be restarted based on a new piecewise linear initial data. Section 5 gives numerical examples to illustrate the effectiveness and efficiency of the front tracking algorithm. We compare the results obtained with the analytical expressions with those obtained using the fifth-order weighted essentially non-oscillatory (WENO) scheme [31]. Section 6 presents some concluding remarks.

2. FORMULATION

2.1. Definition of the problem. As we can postulate, density variation within the concave regime results in the same expressions as those described in Lu et al. [25]. In contrast, density evolution within the convex regime results in the opposite behavior, with a positive jump generating a fan or fans and a negative jump generating a shock structure when the variation of the wave speed is reversed. Nevertheless, the expressions and characteristics of the shock are the same as those in the concave regime. The main task in the construction of the entropy solution is therefore to develop explicit expressions to capture the density variation across the inflection point, where the whole diagram is split into a concave shape on the left and a convex shape on the right.

We consider a homogenous highway that consists of a set of piecewise linear density functions as initial conditions at $t = 0$. The governing equation for the LWR model is the following scalar hyperbolic conservation law

$$\rho_t + f(\rho)_x = 0, \tag{1}$$

where $\rho \in (0, \rho_{jam})$ is the density, ρ_{jam} is the jam density, and $f(\rho)$ is the traffic flow on a homogenous highway. In the literature, $f(\rho)$ is known as the fundamental diagram of road traffic. The relationship among speed u, density ρ, and flow f is

$$f(\rho) = u(\rho)\rho.$$

The flow $f(\rho)$ is considered to be piecewise quadratic, continuous, and not globally concave. Without loss of generality, we focus on the situation in which the flow

$f(\rho)$ is defined by two quadratic functions in different regimes.

$$f(\rho) = \begin{cases} f_1(\rho) & 0 \le \rho < \rho_c, \\ f_2(\rho) & \rho_c \le \rho \le \rho_{jam}, \end{cases}$$

where

$$\text{Flux I}: \ f_1(\rho) = d_0 + d_1\rho + d_2\rho^2; \ \text{Flux II}: \ f_2(\rho) = e_0 + e_1\rho + e_2\rho^2 \tag{2}$$

are different functions that are continuous at the junction $f_1(\rho_c) = f_2(\rho_c)$, concave in Flux I $f_1''(\rho) < 0$, and convex in Flux II $f_2''(\rho) > 0$, and where ρ_c is the critical density that separates the two fluxes. A typical fundamental diagram with this setup is shown in FIGURE 1. The general situation of the fundamental diagram $f(\rho)$ with more than two quadratic functions can be considered using the same procedure for each neighboring pair of quadratic flow functions.

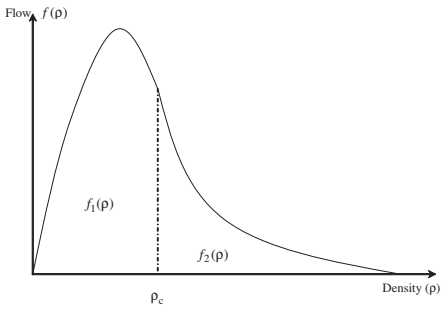

FIGURE 1. A typical fundamental diagram with two quadratic functions (concave on the left, convex on the right) that join continuously at the critical density ρ_c.

We then start to construct explicit solutions to the conservation law with the flows $f(\rho)$ when the initial condition is piecewise linear. We begin with the generalized Riemann problem

$$\rho(x,0) = \begin{cases} \alpha_1 + \beta_{0,1}x & x < 0, \\ \alpha_2 + \beta_{0,2}x & x \ge 0, \end{cases} \tag{3}$$

where the initial density $\alpha_{0,i} + \beta_{0,i}x$ is completely contained in the regime $\rho \le \rho_c$ or $\rho \ge \rho_c$ for $i = 1$ and 2. We again note that we do not need to consider the case in which both linear functions $\alpha_{0,i} + \beta_{0,i}x$ are contained in the same regime $\rho \le \rho_c$ or $\rho \ge \rho_c$, because this case is already covered by the results in Lu et al. [25].

Again, for the scalar conservation law with a quadratic flux $f(\rho) = a + b\rho + c\rho^2$ and a linear initial condition $\rho(x,0) = \alpha_0 + \beta_0 x$, the solution stays linear (see [35]),

$$\rho(x,t) = \alpha(t) + \beta(t)x, \tag{4}$$

with

$$\alpha(t) = \frac{\alpha_0 - b\beta_0 t}{1 + 2c\beta_0 t}, \quad \beta(t) = \frac{\beta_0}{1 + 2c\beta_0 t}. \tag{5}$$

This can be easily obtained using the characteristics method, and we can easily verify that the solution is a smooth fit using the conservation law with the initial condition $\rho(x,0) = \alpha_0 + \beta_0 x$ until the equation becomes singular.

Starting from a particular time (say $t = 0$), the spatial axis is first discretized into a small number of elements, with each pair of adjacent elements being connected by a node. Within each of the pairs the initial density is given by the linear function $\rho(x,0) = \alpha_0 + \beta_0 x$, which is completely contained in the regime $\rho \le \rho_c$ or $\rho \ge \rho_c$. We consider the solution to the generalized Riemann problem (1) with the initial

condition (3) for each of the inner boundary points that separate two piecewise linear initial conditions. The left and right intervals to the inner boundary point under consideration are respectively denoted by $e = (x_l, x_r)$ and $\bar{e} = (\bar{x}_l, \bar{x}_r)$, where $x_r = \bar{x}_l$. The density values of this initial condition at the relevant interval boundaries are denoted by

$$\rho_l = \rho(x_l^+, 0), \quad \rho_r = \rho(x_r^-, 0), \quad \bar{\rho}_l = \rho(\bar{x}_l^+, 0), \quad \bar{\rho}_r = \rho(\bar{x}_r^-, 0).$$

Notice that the exact solution is obtained only to the smallest time when the waves (characteristics or shocks) from the initial condition intersect with one another. It is at this time that the new piecewise linear initial condition is formed and the procedure repeated.

2.2. Natural break time for an element. For an element e in which the wave speed of the initial linear density profile is decreasing, the natural break time (see FIGURE 2) can be determined by the following formula [33].

$$\tau_b = -\frac{1}{f''(\rho)\rho_x}.$$

For an increasing density that falls within the concave regime of the fundamental diagram (i.e., $\rho_x > 0$ and $f''(\rho) < 0$) or a decreasing density that falls within the convex regime (i.e., $\rho_x < 0$ and $f''(\rho) > 0$), the denomination is negative, and thus the wave breaks in a positive finite time. Assuming that the flux function in element e is $f(\rho) = a + b\rho + c\rho^2$, we can obtain the natural break time as $\tau_b = \frac{x_r - x_l}{2c(\rho_l - \rho_r)}$ for $c < 0$ and $\rho_l < \rho_r$, or for $c > 0$ and $\rho_l > \rho_r$.

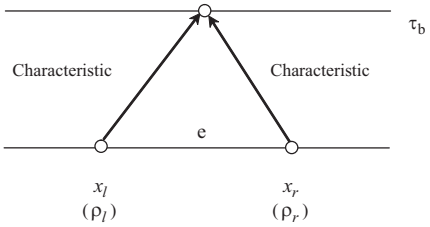

FIGURE 2. Natural break time of an element.

2.3. Propagation of a characteristic. Consider a nodal point between two adjacent elements. When $\rho_r = \bar{\rho}_l$ and $f'_e(\rho_r) = f'_{\bar{e}}(\bar{\rho}_l)$, the density variation is continuous across the elements and a simple characteristic of constant density ρ_r $(= \bar{\rho}_l)$ is generated. The densities on both sides along the characteristic are constant, and the trajectory can be expressed as $x_r + f'_e(\rho_r)t$ or $\bar{x}_l + f'_{\bar{e}}(\bar{\rho}_l)t$ (see FIGURE 3).

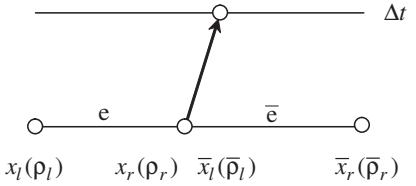

FIGURE 3. Propagation of a characteristic from a nodal point.

2.4. Propagation of a positive-jump shock. If the density jump is contained within the same flux regime, then the analysis and solution given by Wong and Wong [35] and Lu et al. [25] can be used. The case that we are concerned with here is the concave-convex smooth flow diagram with $f_1'' < 0$ and $f_2'' > 0$, as shown

in FIGURE 1. We first consider a positive density jump from ρ_r to $\bar{\rho}_l$ across the critical density ρ_c at a node. As shown in FIGURE 4, we first construct the convex hull of the set $\{(\rho, y)$: $\rho_r \le \rho \le \bar{\rho}_l$ and $y \ge f(\rho)\}$ and use this to find the density pattern that satisfies the Lax entropy condition (see LeVeque [22]).

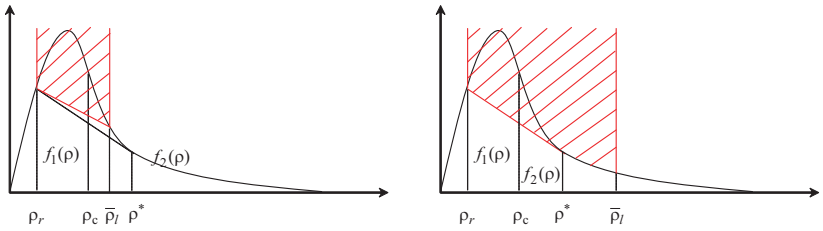

FIGURE 4. Propagation of a characteristic from a nodal point.

We then construct a tangent at the point of tangency $\rho*$ that connects $(\rho_r, f_1(\rho_r))$ and $(\rho*, f_2(\rho*))$. The slope of this tangent is $s* = \frac{f_2(\rho*)-f_1(\rho_r)}{\rho*-\rho_r}$. If $\bar{\rho}_l \le \rho*$, then the shock speed is greater than $s*$, as shown in FIGURE 4, and the positive jump will move as a single shock. In this case, the formulae for the trajectory of the shock and edge densities are identical to those that were derived in Lu et al. [25], although Lu et al. considered both flux functions to be concave, whereas the flux functions in our case are concave-convex.

We then focus on the case $\bar{\rho}_l > \rho*$, the convex hull of which is shown in FIGURE 4. The lower boundary of this set consists of the tangent from $(\rho_r, f_1(\rho_r))$ to $(\rho*, f_2(\rho*))$, and then follows $y = f_2(\rho)$ down to $(\bar{\rho}_l, f_2(\bar{\rho}_l))$. In this case, the tangent represents a shock jumping from ρ_r to $\rho*$, and the remaining segment where the boundary follows $y = f_2(\rho)$ represents a rarefaction wave. As $\rho*$ is the point of tangency, we have $s* = f_2'(\rho*)$, and thus the shock moves at the same speed as the characteristic on this edge of the rarefaction fan.

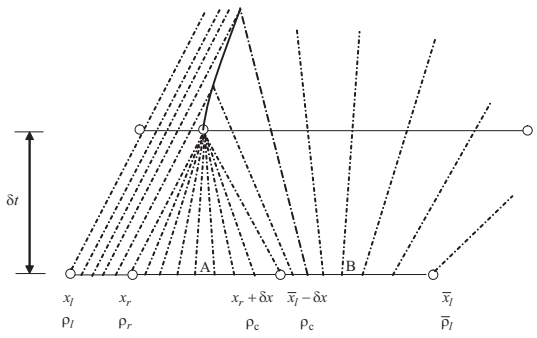

FIGURE 5. The decomposition of a node with a positive density jump across ρ_c into two infinitesimal linear segments.

2.4.1. Explicit trajectory expressions. We now derive the explicit expressions for the trajectories of the shock and rarefaction wave for the case $\bar{\rho}_l > \rho*$. For the expressions for the single shock that is generated in the case $\bar{\rho}_l \le \rho*$, readers are referred to Lu et al. [25].

According to the relationship $s* = f_2'(\rho*)$, we have

$$2e_2\rho* + e_1 = \frac{(e_0 + e_1\rho* + e_2\rho*^2) - (d_0 + d_1\rho_r + d_2\rho_r^2)}{\rho* - \rho_r}.$$

By solving this equation, the tangency density $\rho*$ can be explicitly determined by

$$\rho* = \frac{e_2\rho_r + \sqrt{(e_2\rho_r)^2 + e_2(e_0 - d_0 - d_1\rho_r + e_1\rho_r - d_2\rho_r^2)}}{e_2}.$$

First, x_r and $\tilde{x}_l$ that are initially in the same location are expected to separate each other with $x_r < \tilde{x}_l$ due to the development of two waves between the two adjacent elements, thus we slightly displace the location of the right-hand element to form two infinitesimal linear segments A and B that are separated by the critical density ρ_c and have an equal width δx, as shown in FIGURE 5. Two new virtual elements A and B are thereby generated, each of which belongs to a separate flux regime. For element A with $\rho_r \to \rho_c$ on the concave regime, there is a natural break after δt. The flux functions for elements A and B are $d_0 + d_1\rho + d_2\rho^2$ and $e_0 + e_1\rho + e_2\rho^2$, respectively, where $d_2 < 0$ and $e_2 > 0$. The natural break time δt can therefore be determined by $\frac{\delta x}{2d_2(\rho_r - \rho_c)}$, and the coordinates of these elements after δt then become

$$\tilde{x}_l = x_l + (d_1 + 2d_2\rho_l)\frac{\delta x}{2d_2(\rho_r - \rho_c)}, \tag{6}$$

$$\tilde{x}_r = x_r + (d_1 + 2d_2\rho_r)\frac{\delta x}{2d_2(\rho_r - \rho_c)}, \tag{7}$$

$$\tilde{x}'_l = \bar{x}_l - \delta x + (e_1 + 2e_2\rho_c)\frac{\delta x}{2d_2(\rho_r - \rho_c)} = \tilde{x}_r, \tag{8}$$

$$\tilde{x}'_r = \bar{x}_l + (e_1 + 2e_2\bar{\rho}_l)\frac{\delta x}{2d_2(\rho_r - \rho_c)}. \tag{9}$$

We can deduce the resultant shock trajectory expression using the same method that was adopted in Wong and Wong [35] based on the conservation principle, as illustrated in FIGURE 6. Because $\rho_c > \rho_r$ and element e' belongs to Flux I and $\bar{e}'$ to Flux II, a shock that satisfies the Lax entropy condition is generated from point $\tilde{x}'_l = \tilde{x}_r$ that will move forward or backward along a curve that is determined by the Rankine-Hugoniot jump condition. We here assume that the shock moves forward, such that its location $\tilde{x}'_l + \Delta x$ after time Δt can be determined by the flow conservation in the rectangular region Ω, with $(\tilde{x}'_l, 0)$ and $(\tilde{x}'_l + \Delta x, \Delta t)$ as the end points of the diagonal. As we only consider the time Δt that is earlier than the earliest time when the waves from the initial condition interact with one another, we can safely assume that the left and top boundaries of this rectangle, $\partial\Omega_l$ and $\partial\Omega_t$, belong to Flux I, and the right and bottom boundaries of the rectangle, $\partial\Omega_r$ and $\partial\Omega_b$, belong to Flux II.

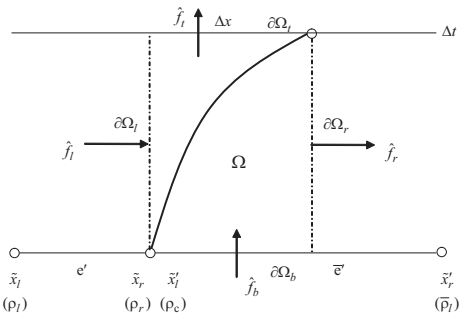

FIGURE 6. Propagation of a right-moving shock from the virtual node.

The flux at the left boundary $\partial\Omega_l$, which is the number of vehicles coming into the region Ω from the left boundary during the period Δt, is

(10)
$$\hat{f}_l = \int_0^{\Delta t} f_1 \mid_{x=\tilde{x}_r} dt = \int_0^{\Delta t} [d_0 + d_1(\alpha_1(t) + \beta_1(t)\tilde{x}_r) + d_2(\alpha_1(t) + \beta_1(t)\tilde{x}_r)^2]dt.$$

Likewise, the flux at the right boundary $\partial\Omega_r$, which is the number of vehicles leaving the region Ω at the right boundary, is

$$\hat{f}_r = \int_0^{\Delta t} f_r \Big|_{x=\tilde{x}'_l} dt = \int_0^{\Delta t} [e_0 + e_1(\alpha_1(t) + \beta_1(t)\tilde{x}'_l) + e_2(\alpha_1(t) + \beta_1(t)\tilde{x}'_l)^2]dt.$$

The initial number of vehicles within region Ω at time $t = 0$ is

$$\hat{f}_b = \int_{\tilde{x}'_l}^{\tilde{x}'_l+\Delta x} (\alpha_2(0) + \beta_2(0)x)dx. \tag{11}$$

The final number of vehicles within region Ω at time $t = \Delta t$ is

$$\hat{f}_t = \int_{\tilde{x}_r}^{\tilde{x}_r+\Delta x} (\alpha_1(0) + \beta_1(0)x)dx. \tag{12}$$

From the flow conservation principle, we deduce that

$$\hat{f}_l - \hat{f}_r + \hat{f}_b - \hat{f}_t = 0.$$

Using (5), we obtain the explicit equation that determines Δx to be

$$F_1(\Delta t)\Delta x^2 + F_2(\Delta t)\Delta x + F_3(\Delta t) = 0, \tag{13}$$

where for the case $\rho_l = \rho_r$,

$$F_1(\Delta t) = \bar{\rho}_l - \rho_c,$$

$$F_2(\Delta t) = 2[e_1(\rho_c - \bar{\rho}_l)\Delta t + 2e_2\rho_r(\rho_c - \bar{\rho}_l)\Delta t + (\rho_r - \rho_c)\delta x],$$

$$\begin{aligned} F_3(\Delta t) = -t\{&[e_1^2 + 4(d_0 - e_0)e_2](\rho_c - \bar{\rho}_l)\Delta t + 2(d_0 - e_0 - e_1\rho_c - e_2\rho_c^2)\delta x \\ &+2d_1\rho_r[2e_2(\rho_c - \bar{\rho}_l)\Delta t + \delta x] + 2d_2\rho_r^2[2e_2(\rho_c - \bar{\rho}_l)\Delta t + \delta x]\}, \end{aligned}$$

and for the case $\rho_l \neq \rho_r$,

$$\begin{aligned} F_1(\Delta t) = &\{2\Delta t(d_2 - e_2)(\rho_r - \rho_l)(\bar{\rho}_l - \rho_c) + (x_r - x_l)(\bar{\rho}_l - \rho_c) - \delta x(\rho_r - \rho_l)\}/ \\ &\{2[2d_2\Delta t(\rho_l - \rho_r) + x_l - x_r][2e_2\Delta t(\rho_c - \bar{\rho}_l) - \delta x]\}, \end{aligned}$$

$$\begin{aligned} F_2(\Delta t) = &\{-(x_l - x_r)[\Delta t(e_1 + 2e_2\rho_r)(\rho_c - \bar{\rho}_l) + (\rho_c - \rho_r)\delta x] \\ &+d_1\Delta t(\rho_l - \rho_r)[2e_2\Delta t(\rho_c - \bar{\rho}_l) - \delta x] \\ &-2d_2\Delta t(\rho_l - \rho_r)[\Delta t e_1(\rho_c - \bar{\rho}_l) + \rho_c\delta x]\}/ \\ &\{[2d_2\Delta t(\rho_l - \rho_r) + x_l - x_r][2e_2\Delta t(\rho_c - \bar{\rho}_l) - \delta x]\}, \end{aligned}$$

$$\begin{aligned} F_3(\Delta t) = &\{\Delta t\{(x_l - x_r)\{\Delta t[e_1^2 + 4(d_0 - e_0)e_2](\rho_c - \bar{\rho}_l) \\ &-2(d_0 - e_0 - e_1\rho_c - e_2\rho_c^2)\delta x\} \\ &+2d_2\{\Delta t^2[e_1^2 + 4(d_0 - e_0)e_2](\rho_l - \rho_r)(\rho_c - \bar{\rho}_l) \\ &+2\Delta t\{e_2[\rho_c\rho_r^2(x_l - x_r) + \rho_r^2\bar{\rho}_l(x_r - x_l) + \rho_c^2(\rho_l - \rho_r)\delta x] \\ &-(d_0 - e_0 - e_1\rho_c)(\rho_l - \rho_r)\delta x\} - \rho_r^2(x_l - x_r)\delta x\} \\ &-d_1^2\Delta t(\rho_l - \rho_r)[2\Delta t e_2(\rho_c - \bar{\rho}_l) - \delta x] \\ &+2d_1\rho_r(x_l - x_r)(2\Delta t e_2(\rho_c - \bar{\rho}_l) - \delta x)\}\}/ \\ &\{2[2d_2\Delta t(\rho_l - \rho_r) + x_l - x_r][2e_2\Delta t(\rho_c - \bar{\rho}_l) - \delta x]\}. \end{aligned}$$

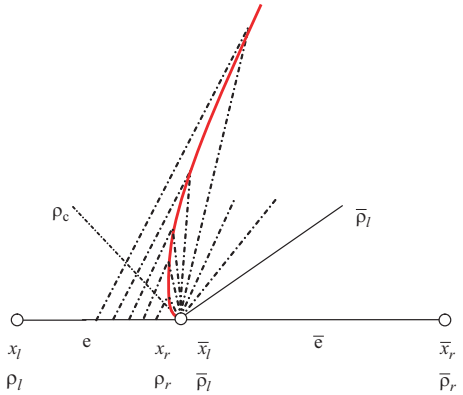

FIGURE 7. Time-space diagram of a positive jump across the critical density at a node.

The shock trajectory can therefore be determined by solving the quadratic equation

$$\Delta x = \frac{-F_2(\Delta t) + \sqrt{F_2^2(\Delta t) - 4F_1(\Delta t)F_3(\Delta t)}}{2F_1(\Delta t)}.$$

Letting $\delta x \to 0$ gives the resultant time-space diagram of a positive density jump across the critical density, as shown in FIGURE 7. The explicit expressions are given as follows.

For the case $\rho_l = \rho_r$,

$$F_1(\Delta t) = \bar{\rho}_l - \rho_c, \tag{14}$$

$$F_2(\Delta t) = 2[e_1(\rho_c - \bar{\rho}_l)\Delta t + 2e_2\rho_r(\rho_c - \bar{\rho}_l)\Delta t], \tag{15}$$

$$\begin{aligned} F_3(\Delta t) = &-\Delta t\{[e_1^2 + 4(d_0 - e_0)e_2](\rho_c - \bar{\rho}_l)\Delta t + 2d_1\rho_r[2e_2(\rho_c - \bar{\rho}_l)\Delta t] \\ &+2d_2\rho_r^2[2e_2(\rho_c - \bar{\rho}_l)\Delta t]\}. \end{aligned} \tag{16}$$

For the case $\rho_l \neq \rho_r$,

$$\begin{aligned} F_1(\Delta t) = &\{2\Delta t(d_2 - e_2)(\rho_r - \rho_l)(\bar{\rho}_l - \rho_c) + (x_r - x_l)(\bar{\rho}_l - \rho_c)\}/ \\ &\{2[2d_2\Delta t(\rho_l - \rho_r) + x_l - x_r][2e_2\Delta t(\rho_c - \bar{\rho}_l)]\}, \end{aligned} \tag{17}$$

$$\begin{aligned} F_2(\Delta t) = &\{-(x_l - x_r)[\Delta t(e_1 + 2e_2\rho_r)(\rho_c - \bar{\rho}_l)] + d_1\Delta t(\rho_l - \rho_r)[2e_2\Delta t(\rho_c - \bar{\rho}_l)] \\ &-2d_2\Delta t(\rho_l - \rho_r)[\Delta te_1(\rho_c - \bar{\rho}_l)]\}/ \\ &\{[2d_2\Delta t(\rho_l - \rho_r) + x_l - x_r][2e_2\Delta t(\rho_c - \bar{\rho}_l)]\}, \end{aligned} \tag{18}$$

$$\begin{aligned} F_3(\Delta t) = &\{\Delta t\{(x_l - x_r)\{\Delta t[e_1^2 + 4(d_0 - e_0)e_2](\rho_c - \bar{\rho}_l)\} \\ &+2d_2\{\Delta t^2[e_1^2 + 4(d_0 - e_0)e_2](\rho_l - \rho_r)(\rho_c - \bar{\rho}_l) \\ &+2\Delta t\{e_2[\rho_c\rho_r^2(x_l - x_r) + \rho_r^2\bar{\rho}_l(x_r - x_l)]\}\} \\ &-d_1^2\Delta t(\rho_l - \rho_r)[2\Delta te_2(\rho_c - \bar{\rho}_l)] + 2d_1\rho_r(x_l - x_r)(2\Delta te_2 \\ &(\rho_c - \bar{\rho}_l))\}\}/\{2[2d_2\Delta t(\rho_l - \rho_r) + x_l - x_r][2e_2\Delta t(\rho_c - \bar{\rho}_l)]\}. \end{aligned} \tag{19}$$

2.4.2. Explicit edge density expressions. We now show the density expressions along the shock generated from the positive jump. From (4) and (5), we have

$$\rho_r(\Delta x^-, \Delta t) = \alpha_1(\Delta t) + \beta_1(\Delta t)(\tilde{x}_r + \Delta x),$$

where $\alpha_1(\Delta t) = \frac{\alpha_{0,1} - d_1\beta_{0,1}\Delta t}{1+2d_2\beta_{0,1}\Delta t}$, $\beta_1(\Delta t) = \frac{\beta_{0,1}}{1+2d_2\beta_{0,1}\Delta t}$, $\alpha_{0,1} = \frac{\tilde{x}_r\rho_l - \tilde{x}_l\rho_r}{\tilde{x}_r - \tilde{x}_l}$, and $\beta_{0,1} = \frac{\rho_r - \rho_l}{\tilde{x}_r - \tilde{x}_l}$, and

$$\bar{\rho}_l(\Delta x^+, \Delta t) = \alpha_2(\Delta t) + \beta_2(\Delta t)(\tilde{x}'_l + \Delta x),$$

where $\alpha_2(\Delta t) = \frac{\alpha_{0,2} - e_1\beta_{0,2}\Delta t}{1+2e_2\beta_{0,2}\Delta t}$, $\beta_2(\Delta t) = \frac{\beta_{0,2}}{1+2e_2\beta_{0,2}\Delta t}$, $\alpha_{0,2} = \frac{\tilde{x}'_r\rho_c - \tilde{x}'_l\bar{\rho}_l}{\tilde{x}'_r - \tilde{x}'_l}$, and $\beta_{0,2} = \frac{\bar{\rho}_l - \rho_c}{\tilde{x}'_r - \tilde{x}'_l}$.

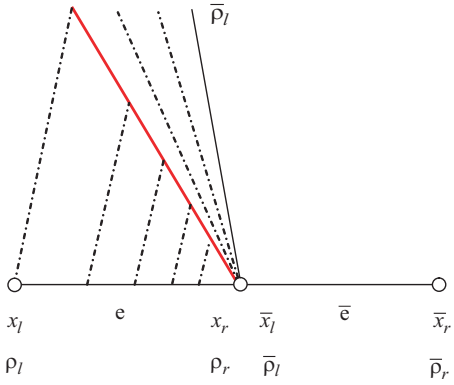

FIGURE 8. Time-space diagram of a positive jump across the critical density at a node with $\rho_l = \rho_r$.

Substituting (6), (7), (8) and (9) into these density functions for case $\rho_l = \rho_r$ gives

$$\rho_r(\Delta x^-, \Delta t) = \rho_r,$$

$$\begin{aligned}\bar{\rho}_l(\Delta x^+, \Delta t) &= \alpha_2(\Delta t) + \beta_2(\Delta t)(\tilde{x}'_l + \Delta x)\\ &= -\tfrac{\Delta t e_1 + \bar{x}_l}{2\Delta t e_2} + \tfrac{1}{2\Delta t e_2}[\bar{x}_l + \Delta t e_1 + 2\Delta t e_2\rho_r\\ &\quad - \tfrac{2\Delta t}{\rho_c - \bar{\rho}_l}\sqrt{e_2(e_0 - d_0 + \rho_r(e_1 - d_1 + (e_2 - d_2)\rho_r))(\rho_c - \bar{\rho}_l)^2}]\\ &= \rho_r - \tfrac{1}{e_2(\rho_c - \bar{\rho}_l)}\sqrt{e_2(e_0 - d_0 + \rho_r(e_1 - d_1 + (e_2 - d_2)\rho_r))(\rho_c - \bar{\rho}_l)^2}.\end{aligned}$$

Note that $\bar{\rho}_l(\Delta x^+, \Delta t)$ is constant in this case. The resultant time-space diagram is shown in FIGURE 8.

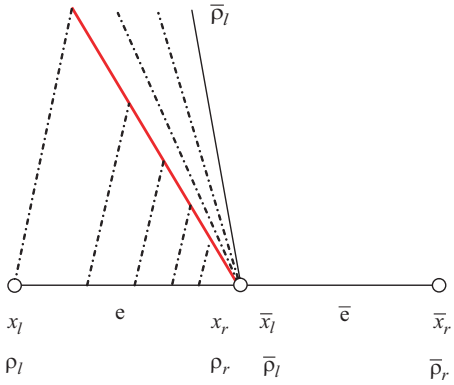

FIGURE 9. Time-space diagram of a positive jump across the critical density at a node with $\rho_l \neq \rho_r$.

For the case $\rho_l \neq \rho_r$,

$$\begin{aligned}\rho_r(\Delta x^-, \Delta t) &= \alpha_1(\Delta t) + \beta_1(\Delta t)(\tilde{x}_r + \Delta x)\\ &= \tfrac{-x_r\rho_l + x_l\rho_r + \Delta t d_1(\rho_r - \rho_l)}{x_l - x_r + 2\Delta t d_2(\rho_l - \rho_r)}\\ &\quad + \tfrac{\rho_l - \rho_r}{x_l - x_r + 2\Delta t d_2(\rho_l - \rho_r)}\left(\bar{x}_l + \tfrac{-F_2(\Delta t) + \sqrt{F_2^2(\Delta t) - 4F_1(\Delta t)F_3(\Delta t)}}{2F_1(\Delta t)}\right),\\ \bar{\rho}_l(\Delta x^+, \Delta t) &= \alpha_2(\Delta t) + \beta_2(\Delta t)(\tilde{x}'_l + \Delta x)\\ &= -\tfrac{\Delta t e_1 + \bar{x}_l}{2\Delta t e_2} + \tfrac{1}{2\Delta t e_2}\left(\bar{x}_l + \tfrac{-F_2(\Delta t) + \sqrt{F_2^2(\Delta t) - 4F_1(\Delta t)F_3(\Delta t)}}{2F_1(\Delta t)}\right),\end{aligned}$$

where the functions $F_1(\Delta t)$, $F_2(\Delta t)$, and $F_3(\Delta t)$ are evaluated by (17)-(19). The resultant time-space diagram is shown in FIGURE 9, in which the right-hand edge density is time dependent.

2.5. Propagation of a negative-jump shock. Similar to Section 2.4, we consider only a negative density jump from ρ_r to $\bar{\rho}_l$ across the critical density ρ_c at a node, where ρ_r and $\bar{\rho}_l$ belong to Flux II and Flux I, respectively. In this sub-section, we construct the convex hull of the set $\{(\rho, y)\colon\ \rho_r \geq \rho \geq \bar{\rho}_l \text{ and } y \leq f(\rho)\}$ for the case $\bar{\rho}_l < \rho*$, because, similar to the cases presented in Section 2.4, the trajectory reduces to a single shock for the case $\bar{\rho}_l \geq \rho*$ and the explicit expressions of the trajectory and edge densities are identical to those given in Lu et al. [25].

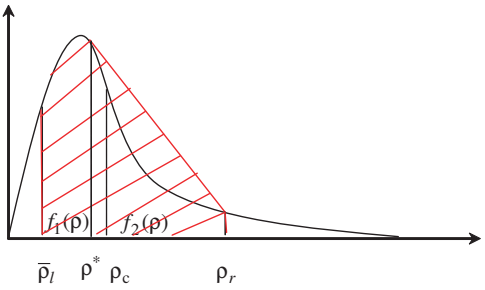

FIGURE 10. Convex hull (shaded region) for $\{(\rho, y)\colon\ \rho_r \geq \rho \geq \bar{\rho}_l \text{ and } y \leq f(\rho)\}$ with $\bar{\rho}_l < \rho^*$.

We now focus on the case $\bar{\rho}_l < \rho*$ and construct the convex hull as shown in FIGURE 10, in which the tangent at $\rho*$ meets the fundamental diagram at ρ_r. This tangent represents a shock that jumps fromρ_r to $\rho*$, and the remaining segment where the boundary follows $f_1(\rho)$ represents a rarefaction wave. According to the relationship $s* = f_1'(\rho*)$, we have

$$2d_2\rho* + d_1 = \frac{(d_0 + d_1\rho* + d_2\rho*^2) - (e_0 + e_1\rho_r + e_2\rho_r^2)}{\rho* - \rho_r}. \tag{20}$$

The tangential density $\rho*$ can be directly determined by solving (20) to give

$$\rho* = \frac{d_2\rho_r + \sqrt{(d_2\rho_r)^2 - d_2(e_0 - d_0 - d_1\rho_r + e_1\rho_r + e_2\rho_r^2)}}{d_2}.$$

Using the same approach as that discussed in Section 2.4, the explicit expressions for the evolution of a negative jump in time and space are shown as follows. The trajectory of the shock is

$$\Delta x = \frac{-F_2(\Delta t) + \sqrt{F_2^2(\Delta t) - 4F_1(t)F_3(\Delta t)}}{2F_1(\Delta t)}.$$

For the case $\rho_l = \rho_r$, we have

$$F_1(\Delta t) = \bar{\rho}_l - \rho_c,$$

$$F_2(\Delta t) = 2[d_1(\rho_c - \bar{\rho}_l)\Delta t + 2d_2\rho_r(\rho_c - \bar{\rho}_l)\Delta t],$$
$$F_3(\Delta t) = -\Delta t\{[d_1^2 + 4(e_0 - d_0)d_2](\rho_c - \bar{\rho}_l)\Delta t + 2e_1\rho_r[2d_2(\rho_c - \bar{\rho}_l)\Delta t] + 2e_2\rho_r^2[2d_2(\rho_c - \bar{\rho}_l)\Delta t]\},$$

and the edge densities

$$\rho_r(\Delta x^-, \Delta t) = \rho_r,$$
$$\begin{aligned}\bar{\rho}_l(\Delta x^+, \Delta t) &= \alpha_2(\Delta t) + \beta_2(\Delta t)(\tilde{x}_l' + \Delta x)\\ &= -\tfrac{\Delta t d_1 + \bar{x}_l}{2\Delta t d_2} + \tfrac{1}{2\Delta t d_2}[\bar{x}_l + \Delta t d_1 + 2\Delta t d_2\rho_r\\ &\quad - \tfrac{2\Delta t}{\rho_c - \bar{\rho}_l}\sqrt{d_2(d_0 - e_0 + \rho_r(d_1 - e_1 + (d_2 - e_2)\rho_r))(\rho_c - \bar{\rho}_l)^2}]\\ &= \rho_r - \tfrac{1}{d_2(\rho_c - \bar{\rho}_l)}\sqrt{d_2(d_0 - e_0 + \rho_r(d_1 - e_1 + (d_2 - e_2)\rho_r))(\rho_c - \bar{\rho}_l)^2}.\end{aligned}$$

The resultant time-space diagram of this negative density jump is shown in FIGURE 11.

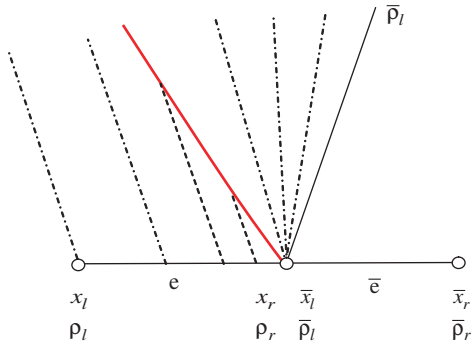

FIGURE 11. Time-space diagram of a negative jump across the critical density at a node with $\rho_l = \rho_r$.

For the case $\rho_l \neq \rho_r$, we have

$$F_1(\Delta t) = \{2\Delta t(e_2 - d_2)(\rho_r - \rho_l)(\bar{\rho}_l - \rho_c) + (x_r - x_l)(\bar{\rho}_l - \rho_c)\}/\{2[2e_2\Delta t(\rho_l - \rho_r) + x_l - x_r][2d_2\Delta t(\rho_c - \bar{\rho}_l)]\},$$

$$F_2(\Delta t) = \{-(x_l - x_r)[\Delta t(d_1 + 2d_2\rho_r)(\rho_c - \bar{\rho}_l)] + e_1\Delta t(\rho_l - \rho_r)[2d_2\Delta t(\rho_c - \bar{\rho}_l)] - 2e_2\Delta t(\rho_l - \rho_r)[\Delta t d_1(\rho_c - \bar{\rho}_l)]\}/\{[2e_2\Delta t(\rho_l - \rho_r) + x_l - x_r][2d_2\Delta t(\rho_c - \bar{\rho}_l)]\},$$

$$F_3(\Delta t) = \{\Delta t\{(x_l - x_r)\{\Delta t[d_1^2 + 4(e_0 - d_0)d_2](\rho_c - \bar{\rho}_l)\} + 2e_2\{\Delta t^2[d_1^2 + 4(e_0 - d_0)d_2](\rho_l - \rho_r)(\rho_c - \bar{\rho}_l) + 2\Delta t\{d_2[\rho_c\rho_r^2(x_l - x_r) + \rho_r^2\bar{\rho}_l(x_r - x_l)]\}\} - e_1^2\Delta t(\rho_l - \rho_r)[2\Delta t d_2(\rho_c - \bar{\rho}_l)] + 2e_1\rho_r(x_l - x_r)(2\Delta t d_2(\rho_c - \bar{\rho}_l))\}\}/\{2[2e_2\Delta t(\rho_l - \rho_r) + x_l - x_r][2d_2\Delta t(\rho_c - \bar{\rho}_l)]\}$$

and the edge densities

$$\begin{aligned}\rho_r(\Delta x^-, \Delta t) &= \alpha_1(\Delta t) + \beta_1(\Delta t)(\tilde{x}_r + \Delta x)\\ &= \tfrac{-x_r\rho_l + x_l\rho_r + \Delta t e_1(\rho_r - \rho_l)}{x_l - x_r + 2\Delta t e_2(\rho_l - \rho_r)}\\ &\quad + \tfrac{\rho_l - \rho_r}{x_l - x_r + 2\Delta t e_2(\rho_l - \rho_r)}\left(x_r + \tfrac{-F_2(\Delta t) + \sqrt{F_2^2(\Delta t) - 4F_1(\Delta t)F_3(\Delta t)}}{2F_1(\Delta t)}\right),\end{aligned}$$

$$\begin{aligned}\bar{\rho}_l(\Delta x^+, \Delta t) &= \alpha_2(\Delta t) + \beta_2(\Delta t)(\tilde{x}_l' + \Delta x)\\ &= -\tfrac{\Delta t d_1 + \bar{x}_l}{2\Delta t d_2} + \tfrac{1}{2\Delta t d_2}\left(\bar{x}_l + \tfrac{-F_2(\Delta t) + \sqrt{F_2^2(\Delta t) - 4F_1(\Delta t)F_3(\Delta t)}}{2F_1(\Delta t)}\right).\end{aligned}$$

The resultant time-space diagram of this negative density is shown in FIGURE 12.

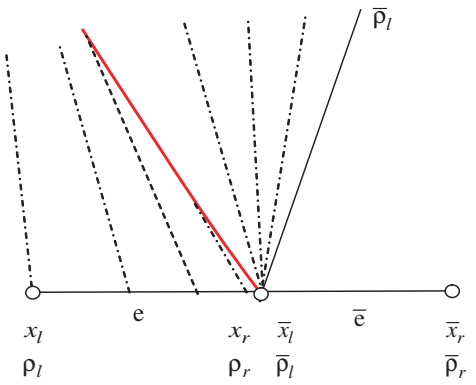

FIGURE 12. Time-space diagram of a negative jump across the critical density at a node with $\rho_l \neq \rho_r$.

3. BOUNDARY CONDITIONS

3.1. Highway entrance. In this part, we focus on the boundary condition at the left boundary $x = 0$, which is the highway entrance. From solution (4)-(5), we can see that the general solution with a linear initial condition is not linear in t for a fixed x unless $\beta = 0$, in which case the solution is constant in t. Therefore, within our piecewise linear (in space) framework, we can only consider the piecewise constant boundary conditions for an exact solution. A typical boundary condition at $x = 0$ that is commonly used for engineering applications is shown in FIGURE 13.

We need to consider the situation in which ρ_r and the linear function in the first interval with end values $\bar{\rho}_l$ and $\bar{\rho}_r$ belong to different regimes in 2, as otherwise the solution is the same as that given in Lu et al. [25].

When $\rho_r < \rho_c < \bar{\rho}_l$, the coefficient in the quadratic equation (13) is the same as the coefficients listed in Section 2.4. Similarly, when $\bar{\rho}_l < \rho_c < \rho_r$ the solution can be determined using the expressions in Section 2.5.

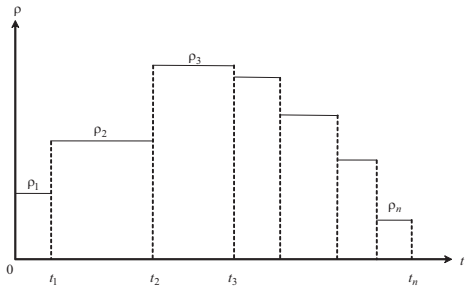

FIGURE 13. A typical boundary condition at the highway entrance $x = 0$.

3.2. Highway exit. In this section, we discuss the boundary conditions at the right boundary $x = x_{end}$, which is the highway exit. We consider a typical exit setup with a traffic light that switches between red and green lights. This is similar to the piecewise constant boundary condition considered for the entrance in the

previous sub-section. The constant values of the density for the green and red lights are $\bar{\rho}_l = 0$ and $\bar{\rho}_l = \rho_{jam}$, respectively.

When $\bar{\rho}_l = \rho_{jam}$, which corresponds to a red light, a left-moving shock is generated. We again only consider $\rho_r < \rho_c < \bar{\rho}_l$, which is the situation in which the density at the left of x_{end} belongs to the regime of Flux I in 2. The value Δx that determines the discontinuity location $x_{end} + \Delta x$ after time Δt is given by (13). The right flux $\widehat{f}_r$ in (10) is then simplified to

$$\widehat{f}_r = 0,$$

and the bottom flux $\widehat{f}_b$ in (12) is simplified to

$$\widehat{f}_b = \rho_{jam}\Delta x.$$

The coefficients in the quadratic equation (13) can thus be simplified to

$$\tilde{F}_1(\Delta t) = \rho_{jam} - \rho_c,$$

$$\tilde{F}_2(\Delta t) = 2[e_1(\rho_c - \rho_{jam})\Delta t + 2e_2\rho_r(\rho_c - \rho_{jam})\Delta t],$$

$$\begin{aligned}\tilde{F}_3(\Delta t) = -\Delta t\{&[e_1^2 + 4(d_0 - e_0)e_2](\rho_c - \rho_{jam})\Delta t + 2d_1\rho_r[2e_2(\rho_c - \rho_{jam})\Delta t] \\ &+2d_2\rho_r^2[2e_2(\rho_c - \rho_{jam})\Delta t]\}.\end{aligned}$$

When$\bar{\rho}_l = 0$, which corresponds to a green light, the situation that concerns us is $\bar{\rho}_l < \rho_c < \rho_r$, in which the density at the left of x_{end} belongs to the regime of Flux II in 2, and the trajectory described in Section 2.5 is formed. The expression of the resultant discontinuity can be simplified to

$$\tilde{F}_1(\Delta t) = -\rho_c,$$

$$\tilde{F}_2(\Delta t) = 2[e_1\rho_c\Delta t + 2e_2\rho_r\rho_c\Delta t],$$

$$\tilde{F}_3(\Delta t) = -[e_1^2 + 4(d_0 - e_0)e_2]\rho_c\Delta t^2 - 4e_2d_1\rho_r\rho_c\Delta t^2 - 4e_2d_2\rho_r^2\rho_c\Delta t^2.$$

4. SOLUTION PROCEDURE

In this section, we present the solution procedure. We concentrate on determining the earliest time that the waves (characteristic lines or shocks) interact with one another. At this time, the construction of the entropy solution must be restarted based on new piecewise linear initial data. This procedure is repeated until the end of study period is reached.

The x-axis is first divided into several elements, each of which corresponds to a piecewise linear density function. On the t-axis, a number of preset time epochs are set, each of which corresponds to the time points at which the constant density on the highway entrance changes or the traffic signal on the highway exit switches, as shown in FIGURE 14. We start from $t = 0$. For each element, we first calculate the natural break time τ_b. For each node, we consider several cases of wave interactions separately, and then take the smallest time from these cases, which serves as the point at which the solution procedure must be restarted with a new set of piecewise linear initial data.

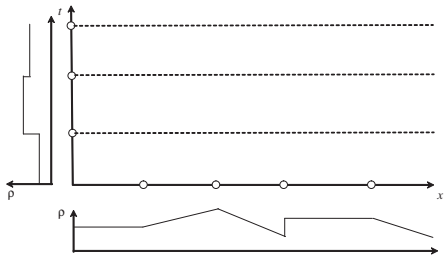

FIGURE 14. Initial spatial discretization and preset time epoch in the solution procedure.

4.1. Intersection between a shock and a characteristic. When two adjacent trajectories are both characteristics, it is easy to calculate their intersection time. For the case of a characteristic intersecting with a shock, we develop a cubic equation to determine the intersection time between the characteristic and shock with a density jump across the critical density. For cases in which the jump of a shock does not include the critical density, the intersection time can be determined using the method in Lu et al. [25], which is also formulated by finding the root of a cubic equation.

We consider the situation in which a characteristic from the element boundary $x_r = \bar{x}_l$ intersects with the shock from the right boundary $\bar{x}_r$. Without loss of generality, we assume that the flux function in the left element is

$$f_1(\rho) = d_0 + d_1\rho + d_2\rho^2$$

and the flux function in the right element is

$$f_2(\rho) = e_0 + e_1\rho + e_2\rho^2.$$

The two trajectories meet at time t, which gives

$$\bar{x}_l + \frac{-F_2(\Delta t) + \sqrt{F_2^2(\Delta t) - 4F_1(\Delta t)F_3(\Delta t)}}{2F_1(\Delta t)} = x_r + (2d_2\rho_l + d_1)\Delta t. \tag{21}$$

By simplifying (21), we obtain

$$\begin{aligned} &(x_l - x_r + 2\Delta t d_2(\rho_l - \rho_r)) \\ &\{[(d_1 - e_1)^2 + 4(d_0 - e_0)e_2 + 4d_2(d_1 - e_1)\rho_l + 4d_2(d_2 - e_2)\rho_l^2]\Delta t^2 \\ &+2(x_l - x_r)(d_1 - e_1 + 2d_2\rho_l - e_2(\rho_l + \rho_r))\Delta t + (x_l - x_r)^2\} = 0. \end{aligned} \tag{22}$$

From (22), we can easily find the roots of the equation. As equation (22) may include some redundant roots that do not satisfy (21), we need to substitute all of the determined roots back into (21) to ascertain the validity of the solutions. We can then determine the earliest intersection point of the characteristic and the shock by choosing the smallest positive feasible root in equation (22). A similar procedure can also be applied for the case of a left-hand shock that interacts with a right-hand characteristic.

4.2. Intersection between two adjacent shocks. This section considers a typical case in which two shocks meet at time t^*, as shown in FIGURE 15. The inner element has two edge densities, ρ_1 on Shock 1 and ρ_2 on Shock 2, at t= 0. The density function along the inner edge is denoted as $D_1(t)$ for Shock 1 and as $D_2(t)$ for Shock 2. Chen et al. [2] showed that the density variation alongside the shock is linear and monotonic, and corresponds to the initial density variation in a hyperbolic system. From the monotonic property of the density variation along the

shock, Chen et al. [2] were able to prove that the two neighboring shocks will intersect if either the rightmost characteristic meets Shock 1 at t_1 or the leftmost characteristic meets Shock 2 at t_2, or both. In this case, the intersection time t^* is less than $\min(t_1, t_2)$ and is unique. An example is shown in FIGURE 16.

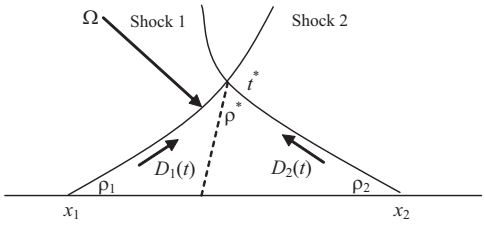

FIGURE 15. Trajectories of two neighboring shocks.

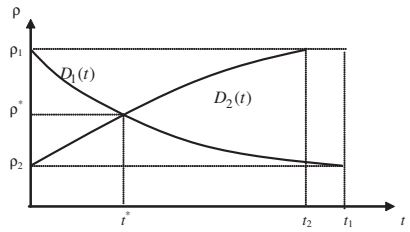

FIGURE 16. The rightmost characteristic meets Shock 1 at time t_1, and the leftmost characteristic meets Shock 2 at time t_2.

We can apply the same rationale as described in Wong and Wong [35] to determine the interaction between two adjacent shocks based on their trajectories. However, the efficiency of the procedure can be further improved using the theorem in Chen et al. [2]. As t_1 and t_2 can be readily found by solving the cubic equation (22), we can efficiently define the search range of the intersection point so that the overall computing time can be reduced. When we encounter scenarios in which the density varies across the critical density within an element at the beginning of the study period, then the x-axis needs to be divided into a number of intervals, the initial density within each of which is given by a linear function $\rho(x, 0) = \alpha + \beta x$ that is completely contained in the regime $\rho \leq \rho_c$ or $\rho \geq \rho_c$. From [2], we know that the density of any element that does not include the critical density will not include the critical density at any future time before it breaks. To determine the trajectory of a density jump across the critical density, we can infer from the density evolution equations that the density along the resultant shock is linear within the range of the initial density span. Hence, the method in [2] can also be used for cases involving such trajectories, as follows.

As the density alongside a shock varies monotonically, when each pair of trajectories intersects, the right-hand edge density of the trajectory on the left is equal to the left-hand edge density of the trajectory on the right. We therefore use the difference between the corresponding edge densities for each pair of trajectories to calculate the intersection point and determine the next renewal time epoch. The search range is $(0, t_s)$, where $t_s = \min(t_1, t_2)$.

Let $D_1(t)$ be the right-hand edge of the trajectory on the left and $D_2(t)$ the left-hand edge of the trajectory on the right, as shown in FIGURE 16. Their explicit expressions are derived in Sections 2.4 and 2.5. Initially, we have $D_1(0) = \rho_l$ and $D_2(0) = \rho_r$ for the element between these two trajectories. We define the

function of density difference as $Z(t) = D_2(t) - D_1(t)$, in which $Z(0)$ and $Z(t_s)$ must take different signs and the root of $Z(t)$ is unique within the range $(0, t_s)$ (see [2]). Without loss of generality, we assume that $Z(0) > 0$ and $Z(t_s) < 0$. The intersection time can then be easily determined using the following procedure.

Step 1: Compute $Z(0) > 0$.

Step 2: Compute $Z(t_s) < 0$.

Step 3: If $Z(t_s) > 0$, then there is no intersection point for this element, and the algorithm terminates; otherwise go to Step 4.

Step 4: Set $t_a = 0$ and $t_b = t_s$.

Step 5: Update $t_s = \frac{Z(t_a)t_b - Z(t_b)t_a}{Z(t_a) - Z(t_b)}$.

Step 6: (1) If $Z(t_s) > \varepsilon$, then set $t_a = t_s$, and go to Step 5.

(2) If $Z(t_s) < -\varepsilon$, then set $t_b = t_s$, and go to Step 5.

(3) If $|Z(t_s)| \leq \varepsilon$, then $t^* = t_s$ is the solution, where ε is a positive precision tolerance.

For the opposite case $Z(0) < 0$ and $Z(t_s) > 0$, the same procedure with slight modification can be used to compute the root.

4.3. Procedure. Starting from $t = 0$, we first determine the earliest preset time Δt (exogenously given and fixed), and then calculate the natural break time, Δt_b^i for each element (if any), as discussed in Section 2.2. For each node, the trajectory of the characteristic or shock emanating from the nodal position at the current time epoch can be deduced from the initial element profiles (see Sections 2.2-2.5). The trajectory of the characteristic or shock from the first node on the left can be determined by the boundary condition of the highway entrance (see Section 3.1), and the boundary meeting time of the last element Δt_{exit} can be obtained using the method in Section 3.2. The intersection time $\Delta t_{m,m+1}$ for each pair of adjacent characteristics or shocks m and $m+1$ is determined using the procedures in Sections 4.1 and 4.2. The next renewal time is then computed as the earliest time of all of these wave interactions by

$$t_{renew} = \min\left(\Delta t, \Delta t_{exit}, \Delta t_b^i, \forall i, t_{m,m+1} \forall m\right).$$

We update the density profile at this renewal time using the explicit expressions developed in the previous sections. The procedure is then repeated until the end of study period is reached.

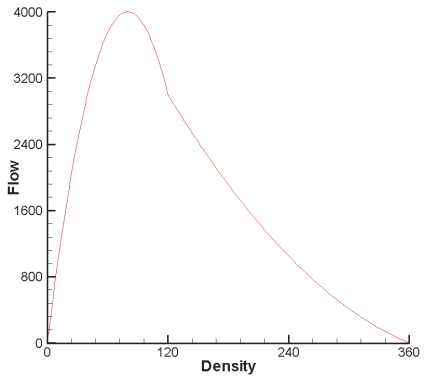

FIGURE 17. The flow-density relationship used in the numerical examples.

5. NUMERICAL EXAMPLES

In this section, we give numerical examples to illustrate the explicit formulae for the entropy solutions obtained in the previous sections. The flow-density relationship is given by

$$f(\rho) = \begin{cases} f_1(\rho) = -0.625\rho^2 + 100\rho, & 0 \le \rho < 120, \\ f_2(\rho) = 0.03125\rho^2 - 27.5\rho + 5850, & 120 \le \rho < 360, \end{cases}$$

which is also shown in FIGURE 17. The first two numerical examples are Riemann problems with the initial conditions

$$\rho(x,0) = \begin{cases} \rho_l, & 0 \le x < 10, \\ \rho_r, & 10 \le x < 20, \end{cases}$$

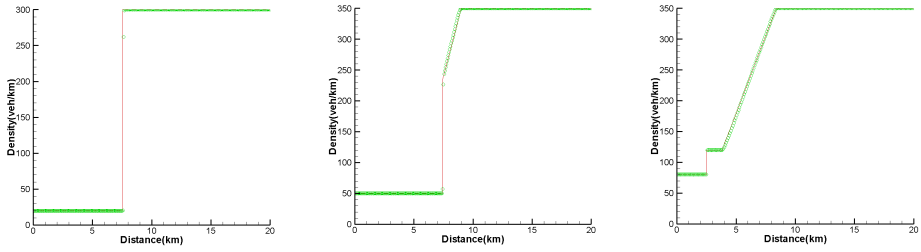

FIGURE 18. The exact entropy solution obtained by the front tracking algorithm (solid line) and the numerical solution derived using the WENO scheme with N = 1000 uniform grid points (circles) for Example 1. Left: case 1-a at $t = 30$ min; middle: case 1-b at $t = 12$ min; right: case 1-c at $t = 18$ min.

5.1. Example 1 (Positive jump). Three typical cases are considered as follows.

Case 1-a: $\rho_l = 20, \rho_r = 300$

In this case, the solution consists of a single shock, as shown in FIGURE 18 (left figure).

Case 1-b: $\rho_l = 50, \rho_r = 350$

In this case, the solution consists of a shock on the left and a rarefaction on the right, as shown in FIGURE 18 (middle figure).

Case 1-c: $\rho_l = 80, \rho_r = 350$

In this case, the solution consists of a shock on the left, a fan of constant critical density in the middle, and a rarefaction on the right, as shown in FIGURE 18 (right figure).

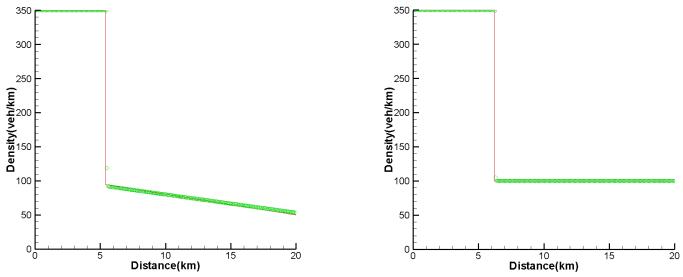

FIGURE 19. The exact entropy solution obtained by the front tracking algorithm (solid line) and the numerical solution derived using the WENO scheme with N = 1000 uniform grid points (circles) for Example 2. Left: case 2-a at $t = 18$ min; right: case 2-b at $t = 15$ min.

5.2. Example 2 (Negative jump). Two typical cases are considered as follows.

Case 2-a: $\rho_l = 350, \rho_r = 50$

In this case, the solution consists of a shock on the left and a rarefaction on the right, as shown in FIGURE 19 (left figure).

Case 2-b: $\rho_l = 350, \rho_r = 100$

In this case, the solution consists of a single shock, as shown in FIGURE 19 (right figure).

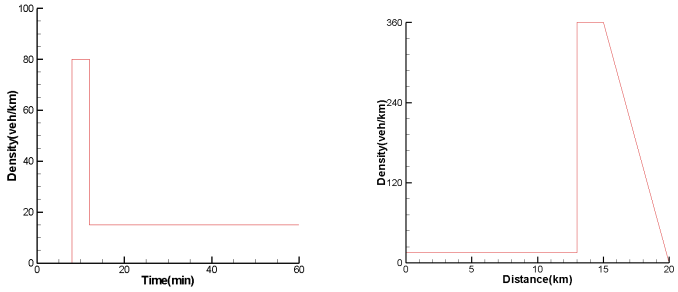

FIGURE 20. Boundary and initial conditions for Example 3. Left: entrance density variation on the time axis at $x = 0$; right: (b) initial density profile on the spatial axis at $t = 0$.

The exact solutions to these problems as worked out using the front tracking procedure are shown as solid lines in FIGURES 18 and 19, and are compared with the numerical solution obtained by the fifth-order WENO scheme [12, 31, 36, 39] using $N = 1000$ uniform grid points, which are shown as circles on the respective figures. We can see that the results agree very well for all of the cases.

TABLE 1. Density functions of the elements at different time epochs for Example 3.
TABLE 2. Compares the computing times of the front tracking algorithm and the WENO scheme (for $N = 5000$), and shows that the WENO scheme requires about 150 times more computation time than the front tracking algorithm.

5.3. Example 3 (Traffic incident). Consider a long homogenous freeway of 20 km in length. The entrance density is 15 veh/km. Due to an incident near the downstream end of the freeway, the traffic density profile that is shown in Figure 20 (left figure) is formed in which a jam-packed condition 2 km long occurs 13 to 15 km from the upstream entrance to the freeway. To release the traffic jam condition downstream, the authority blocks the freeway entrance for 8 minutes, after which traffic is again released from the freeway entrance at a capacity density of 80 veh/km. After 4 minutes, the entrance flow returns to normal with a density of 15 veh/km. The variation in the traffic density at the upstream entrance of the freeway is illustrated in FIGURE 20 (right figure).

Time (min)	Element	x_l(km)	x_r(km)	ρ_l(veh/km)	ρ_r(veh/km)
8.0	1	0.000	12.083	0.0	15.0
	2	12.083	12.474	15.0	15.0
	3	12.474	14.333	360.0	360.0
	4	14.333	15.070	360.0	227.4
	5	15.070	20.000	101.2	73.8
8.248	1	0.000	0.414	80.0	0.0
	2	0.414	12.458	0.0	0.0
	3	12.458	14.313	360.0	360.0
	4	14.313	14.988	360.0	232.5
	5	14.988	20.000	101.0	74.0
11.494	1	0.000	5.824	80.0	0.0
	2	5.824	12.458	0.0	0
	3	12.458	14.042	360.0	360.0
	4	14.042	20.000	99.1	75.6
12.0	1	0.000	6.667	80.0	0.0
	2	6.667	12.458	0.0	0.0
	3	12.458	13.920	360.0	360.0
	4	13.920	20.000	98.8	75.8
15.475	1	0.000	2.718	15.0	15.0
	2	2.718	12.458	62.5	0.0
	3	12.458	13.081	360.0	360.0
		13.081	20.000	97.3	76.7
18.958	1	0.000	5.874	15.0	15.0
	2	5.874	12.237	54.3	26.4
	3	12.237	20.000	96.3	77.3
28.570	1	0.000	15.572	15.0	15.0
	2	15.572	20.000	85.4	78.2
35.300	1	0.000	20.000	15.0	15.0

Method	Example 3		Example 4	
	Time steps	Computing time	Time steps	Computing time
Front tracking	7	2 seconds	144	7 seconds
WENO	20834	308 seconds	20691	347 seconds

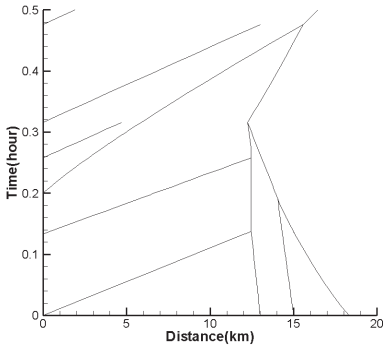

FIGURE 21. Time-space diagram of evolution waves for Example 3.

The solution is shown in TABLE 1, and the space-time diagram of the waves involved is illustrated in FIGURE 21. FIGURE 22 shows the exact solution to the problem as worked out using the expressions developed in the foregoing section (shown as solid lines), and compares it with a numerical solution obtained using the

fifth order WENO scheme using N = 5000 uniform grid points (shown as circles). We can again see that the two outcomes agree quite well. From these figures, we can clearly observe the formation of a wide moving jam with two very sharp shock fronts at both ends, which is a traffic phenomenon that is commonly observed on highways and well studied [13, 18–20, 24, 37, 38].

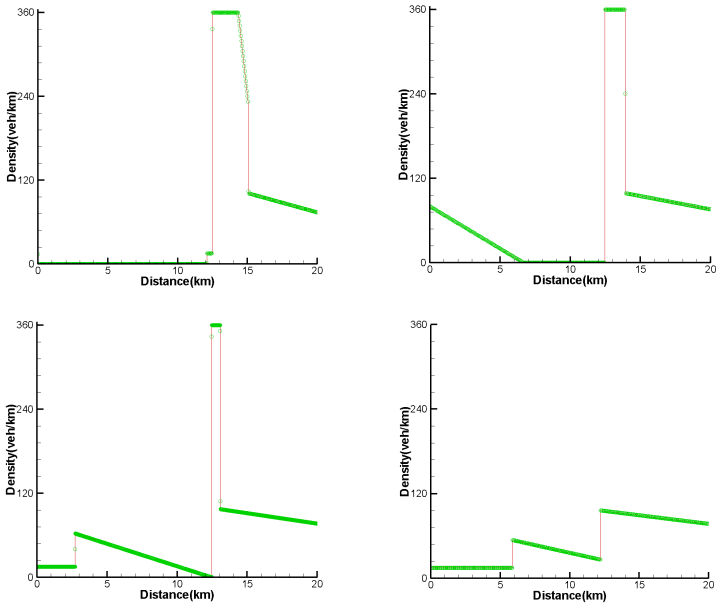

FIGURE 22. The exact entropy solution obtained by the front tracking algorithm (solid line) and the numerical solution derived using the WENO scheme with N = 5000 uniform grid points (circles) for Example 3. Top left: $t = 8$ min; top right: $t = 12$ min; bottom left: $t = 15.475$ min; bottom right: $t = 18.958$ min.

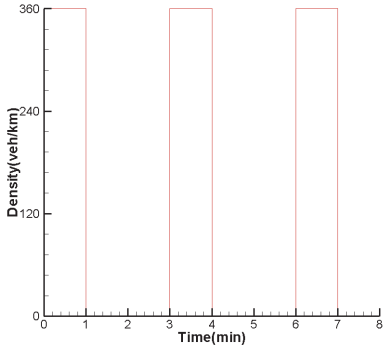

FIGURE 23. Periodic signal settings at the highway exit for Example 4.

5.4. Example 4 (Signal control). This example shares the same initial condition and entrance boundary condition as those described in Example 3. However, at the exit boundary, a traffic signal is installed with a repeated pattern of 1 minute of red light followed by 2 minutes of green light, as shown in FIGURE 23. The exact solution to this problem is again worked out using the expressions developed in the foregoing section, and is shown as solid lines in FIGURE 24. This solution is then compared with the numerical solution obtained using the WENO scheme

and N = 5000 uniform grid points, which is shown as circles in the figure. We can again see that the two outcomes agree quite well. The computing times are also shown in TABLE 2, from which we can see that the WENO scheme requires about 50 times more computing time than the front tracking algorithm.

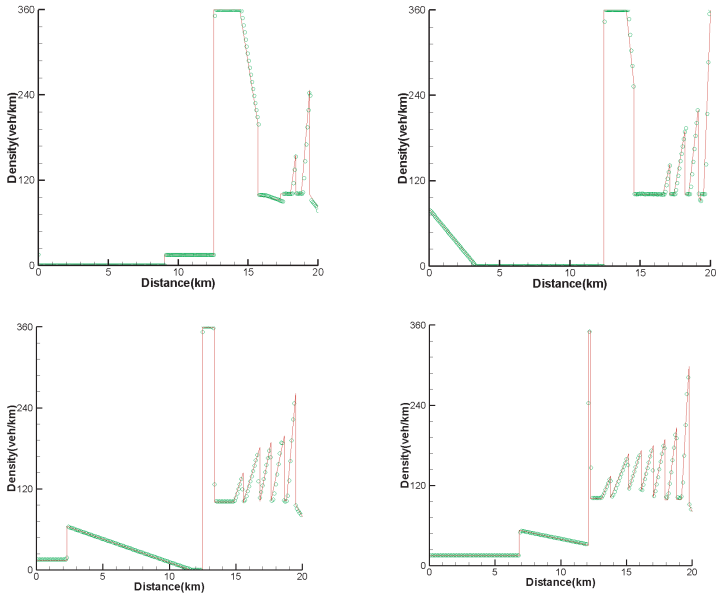

FIGURE 24. The exact entropy solution obtained by the front tracking algorithm (solid line) and the numerical solution derived using the WENO scheme with N = 5000 uniform grid points (circles) for Example 4. Top left: t = 6 min; top right: t = 10 min; bottom left: t = 15 min; bottom right: t = 20min.

6. CONCLUSION

In this paper, we have adopted the piecewise quadratic, continuous, non-smooth, and non-concave fundamental diagram in a front tracking algorithm for the LWR model. The algorithm is found to be more flexible in its ability to fit well with observed data, which results in a more realistic traffic flow model to describe traffic movement on highways. Explicit expressions for the path trajectory of the density jump across the critical density have been derived, and the solution procedure is outlined. Several numerical examples have been presented to demonstrate the effectiveness of the constructed entropy solutions for both simple Riemann initial conditions and representative traffic flow problems. A comparison of the results from the front tracking algorithm with numerical solutions obtained using a fifth-order WENO scheme shows the front tracking algorithm to be more efficient than a finite-difference scheme, and indicates that it has promising applications for solving traffic flow problems. We also note that although we use traffic flow problems to demonstrate the solution algorithm, it can also be used to solve general scalar conservation equations with piecewise quadratic flux functions.

References

[1] E. Aulisa, S. Manservisi and R. Scardovelli, A novel representation of the surface tension force for two-phase flow with reduced spurious currents, Computer Methods in Applied Mechanics and Engineering 195 (2006) 6239-6257.

[2] W. Chen, S.C. Wong and C.W. Shu, Efficient implementation of the shock-fitting algorithm for the Lighthill-Whitham-Richards traffic flow model, International Journal for Numerical Methods in Engineering 74 (2008) 554-600.
[3] C.M. Dafermos, Polygonal approximations of solutions of the initial value problem for a conservation law, Journal of Mathematical Analysis and Applications 38 (1972) 33-41.
[4] J.S. Drake, J.L. Schofer and A.D. May, A statistical analysis of speed density hypotheses, Highway Research Record 154, Highway Research Board, NRC, Washington D.C., 1967, 53-87.
[5] D. Helbing, Theoretical foundation of macroscopic traffic models, Physica A 219 (1995) 375-390.
[6] V. Henn, A wave-based resolution scheme for the hydrodynamic LWR traffic flow model, in: S.P. Hoogendoorn, S. Luding, P.H.L. Bovy, M. Schreckenberg and D.E. Wolf (Eds.), Traffic and Granular Flow'03. Springer Verlag, 2005, 105-124.
[7] V. Henn, Tracking waves for modelling the impact of incidents, 10th EWGT Meeting and 16th Mini-Euro Conference, Poznan, Pologne, 2005.
[8] H. Holden and L. Holden, On scalar conservation laws in one-dimension, in: S. Albeverio, J.E. Fenstad, H. Holden and T. Lindstroeem (Eds.), Ideas and Methods in Mathematics and Physics. Cambridge Univ. Press, Cambridge, 1998, 480-509.
[9] H. Holden, L. Holden and R. Hoeegh-Krohn, A numerical method for first order nonlinear scalar conservation laws in one-dimension, Computers and Mathematics with Applications 15 (1998) 595-602.
[10] H. Holden and N.H. Risebro, Front Tracking for Hyperbolic Conservation Laws. Volume 152, Applied Mathematical Sciences, Springer, 2002.
[11] E.J. Holm and H.P. Langtangen, A unified finite element method for the injection molding process, Computer Methods in Applied Mechanics and Engineering 178 (1999) 413-429.
[12] G.S. Jiang and C.W Shu, Efficient implementation of weighted ENO schemes, Journal of Computational Physics 126 (1996) 202-228.
[13] W.L. Jin and H.M. Zhang, The formation and structure of vehicle clusters in the Payne-Whitham traffic flow model, Transportation Research Part B 37 (2003) 207-223.
[14] K.H. Karlsen and N.H. Risebro, Corrected operator splitting for nonlinear parabolic equations, SIAM Journal on Numerical Analysis 37 (2000) 980-1003.
[15] K.H. Karlsen, K. Brusdal, K.H. Dahle, S. Evje and K.A. Lie, The corrected operator splitting approach applied to a nonlinear advection-diffusion problem, Computer Methods in Applied Mechanics and Engineering 167 (1998) 239-260.
[16] K.H. Karlsen, K.A. Lie, J.R. Natvig, H.F. Nordhaug and H.K. Dahle, Journal of Computational Physics 173 (2001) 636-663.
[17] K.H. Karlsen, N.H. Risebro and J.D. Towers, Front tracking for scalar balance equations, Journal of Hyperbolic Differential Equations 1 (2004) 115-148.
[18] B.S. Kerner, The Physics of Traffic. Springer, Berlin, New York, 2004.
[19] B.S. Kerner and P. Konhaeuser, Structure and parameters of clusters in traffic flow, Physical Review E 50 (1994) 54-83.
[20] B.S. Kerner and H. Rehborn, Experimental properties of complexity in traffic flow, Physics Review E 53 (1996) R4275-R4278.
[21] M. Kunick, A solution formula for a non-convex scalar hyperbolic conservation law with monotone initial data. Mathematical Methods in the Applied Sciences 16 (1993) 895-902.
[22] R.J. LeVeque, Numerical Methods for Conservation Laws. Lecture in Mathematics, ETH Zurich, Birkhauser Verlag, Basel, Switzerland, 1992.
[23] M.J. Lighthill and F.B. Whitham, On kinetic wave II: a theory of traffic flow on crowded roads, Proceedings of Royal Society Series A 229 (1955) 317-345.
[24] W. Lin and H.K. Lo, A theoretical probe of a German experiment on stationary moving traffic jams, Transportation Research Part B 37 (2003) 251-261.
[25] Y. Lu, S.C. Wong, M.P. Zhang, C.W. Shu and W. Chen, Explicit construction of entropy solutions for the Lighthill-Whitham-Richards traffic flow model with a piecewise quadratic flow-density relationship. Transportation Research Part B 42 (2008) 355-372.
[26] B.J. Lucier, A moving mesh numerical method for hyperbolic conservation laws, Mathematics of Computation 46 (1986), 59-69.
[27] G.F. Newell, A simplified theory of kinematic waves in highway traffic, Part I: general theory, Transportation Research Part B 27 (1993) 281-287.
[28] G.F. Newell, A simplified theory of kinematic waves in highway traffic, Part II: queuing at freeway bottlenecks, Transportation Research Part B 27 (1993) 289-303.
[29] G.F. Newell, A simplified theory of kinematic waves in highway traffic, Part III: multi-destination flows, Transportation Research Part B 27 (1993) 305-313.

[30] P.I. Richards, Shock waves on the highway, Operations Research 4 (1956) 42-51.
[31] C.W. Shu, Essentially non-oscillatory and weighted essentially non-oscillatory schemes for hyperbolic conservation laws, in: B. Cockburn, C. Johnson, C.W. Shu, and E. Tadmor (Eds), Advanced Numerical Approximation of Nonlinear Hyperbolic Equations. Lecture Notes in Mathematics (Editor: A. Quarteroni), Volume 1697, Springer, 1998, 325-432.
[32] R.T. Underwood, Speed, Volume, and Density Relationships: Quality and Theory of Traffic Flow. Yale Bureau of Highway Traffic, 1961, 141-188.
[33] G.B. Whitham, Linear and Nonlinear Waves. Wiley, New York, 1974.
[34] G.C.K. Wong and S.C. Wong, A multi-class traffic flow model – an extension of LWR model with heterogeneous drivers, Transportation Research Part A 36 (2002) 827-841.
[35] S.C. Wong and G.C.K. Wong, An analytical shock-fitting algorithm for LWR kinematic wave model embedded with linear speed-density relationship, Transportation Research Part B 36 (2002) 683-706.
[36] M. Zhang, C.W. Shu, G.C.K. Wong and S.C. Wong, A weighted essentially non-oscillatory numerical scheme for a multi-class Lighthill-Whitham-Richards traffic flow model, Journal of Computational Physics 191 (2003) 639-659.
[37] P. Zhang and S.C. Wong, Essence of conservation forms in the traveling wave solutions of higher-order traffic flow models, Physical Review E 74 (2006) 026109.
[38] P. Zhang, S.C. Wong and S.Q. Dai, Characteristic parameters of a wide cluster in a higher-order traffic flow model, Chinese Physics Letters 23 (2006) 516-519.
[39] P. Zhang, S.C. Wong and C.W. Shu, A weighted essentially non-oscillatory numerical scheme for a multi-class traffic flow model on an inhomogeneous highway, Journal of Computational Physics 212 (2006) 739-756.

Department of Civil Engineering, The University of Hong Kong, Pokfulam Road, Hong Kong, China
E-mail: manyen@hku.hk and hhecwsc@hkucc.hku.hk
URL: http://web.hku.hk/ hhecwsc

Division of Applied Mathematics, Brown University, Providence, RI 02912, USA
E-mail: shu@dam.brown.edu
URL: http://www.dam.brown.edu/people/shu

Shanghai Institute of Applied Mathematics and Mechanics, Shanghai University, Shanghai, China
E-mail: pzhang@mail.shu.edu.cn
URL: http://pengzg.googlepages.com/pengzhang